WPMAT-PR(18) 21597

PW Ma et al.

Symmetry broken self interstitial atom defects in chromium, molybdenum and tungsten

Preprint of Paper to be submitted for publication in
Physical Review X

This work has been carried out within the framework of the EUROfusion Consortium and has received funding from the Euratom research and training programme 2014-2018 under grant agreement No 633053. The views and opinions expressed herein do not necessarily reflect those of the European Commission.

Symmetry broken self interstitial atom defects in chromium, molybdenum and tungsten

Pui-Wai Ma* and S. L. Dudarev
UK Atomic Energy Authority, Culham Science Centre, Oxfordshire OX14 3DB, United Kingdom

Diffuse x-ray scattering experiments near the Bragg peak (or Huang scattering) suggested a self-interstitial atom (SIA) in Mo adopts a ⟨110⟩ dumbbell configuration. No matter it migrates through a three dimensional or two dimensional pathway, it is contradicting to electron irradiated resistivity experiment that a sub-stage of the stage I temperatures, corresponding to the long range SIA migration, of group 6 elements of periodic table are relatively low. On the other hand, the migration temperatures are too high if one adopts the prediction from density function calculations that ⟨111⟩ dumbbell is the most stable configuration. We performed density functional calculations showing that a SIA adopts a canted dumbbell configuration in all the metals of group 6: chromium, molybdenum and tungsten. A canted structure of the defect can be classified as an ⟨11ξ⟩ dumbbell, where ξ is an irrational number. The fact that the formation energy of a canted configuration is lower than that of a straight ⟨111⟩ defect structure is confirmed by nudged elastic band analyses of the [110] to [111] configuration transformations. We simulated the Huang scattering patterns of different dumbbell configurations. The patterns of ⟨11ξ⟩ dumbbell resembling the patterns of ⟨110⟩, which causes confusion in experiments. A ⟨11ξ⟩ dumbbell migrates through the lattice following a sequence of three-dimensional [11ξ] to [ξ11] transitions. It explains the elastic after effect experiment that no large non-elastic relaxation process was detected during SIA migration in Mo. Calculated barriers for defect migration in non-magnetic Cr, anti-ferromagnetic Cr, Mo and W are 0.052, 0.075, 0.064 and 0.040 eV, respectively. They are well correlated with the migration temperatures observed experimentally.

I. INTRODUCTION

The group 6 elements of the periodic table chromium, molybdenum and tungsten are transition metals of profound technological significance. Cr is an indispensable component of stainless steels, preventing corrosion through passivation. It also improves the resistance to swelling of ferritic-martensitic steels exposed to irradiation [1]. Mo and W, and their alloys, are refractory metals with high melting points, mechanically stable at high temperature. This makes them suitable for a variety of high temperature applications [2, 3], e.g. Mo-25%Re alloys are used in rocket engine components [4]. W is a candidate material for the divertor and first wall in the current fusion power plant design [5, 6].

Mechanical properties of metallic materials strongly depend on their microstructure [7]. To model how the microstructure of Cr, Mo, W and their alloys evolves under irradiation, one needs to know the structure and thermally activated mobility parameters of self-interstitial atom (SIA) defects. Huang scattering experiments [8, 9] suggested that the SIA in Mo adopts a ⟨110⟩ configuration, which is compatible to a scattering pattern showing an orthorhombic displacement field. However, literature data based on density function theory (DFT) calculations suggest that SIAs in all the body-centre cubic transition metals, with the exception of ferromagnetic iron, adopt a linear straight ⟨111⟩ dumbbell or crowdion configuration [10–12].

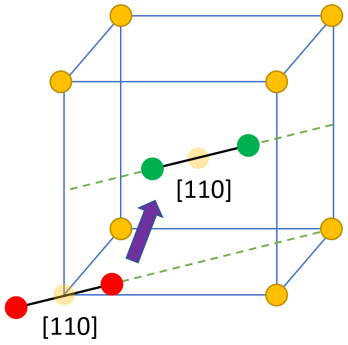

FIG. 1. Schematic picture on two dimensional diffusion of a ⟨110⟩ dumbbell proposed by Jacques and Robrock [13].

According to the resistivity recovery experiments performed on electron irradiated materials [14, 15], the a substage of stage I temperature, corresponding to the long range migration temperature of SIA T_m^{SIA} in Cr, Mo and W are 40K, 35K, and 27K, whereas many other BCC transition metals are characterized by T_m^{SIA} values below 6K, which is the low temperature limit accessible to observations. If an SIA adopts a ⟨110⟩ dumbbell configuration, no matter it migrates in a three dimensional translational-rotational migration as in iron [16], or a jump-step wise two dimensional diffusion as suggested by Jacques and Robrock [13] (Fig. 1), if we consider Fe as a benchmark with T_m^{SIA} = 120K, the experimental values for group 6 elements are comparatively low. If an SIA adopts a ⟨111⟩ dumbbell configuration and diffuses one-dimensionally along the ⟨111⟩ crystallographic directions [17], it implies extremely low T_m^{SIA} characterizing

* Leo.Ma@ukaea.uk

the onset of SIA defect migration in *all* the bcc metals. It turns out that the T_m^{SIA} of group 6 elements are too high.

Fitzgerald and Nguyen-Manh [17] argued that the relatively high values of T_m^{SIA} in group 6 elements are due to the double peak structure of the $\langle 111 \rangle$ inter-atomic-string potential, which affected the Peierls barrier for SIA migration. The argument was based on the analysis of solutions of a constrained, purely one-dimensional, Frenkel-Kontorova model, parameterized from DFT calculations. No direct calculation of SIA migration barriers or investigation of possible deviations from a purely one-dimensional mode of migration was undertaken.

A recent direct DFT nudged elastic band (NEB) calculation showed that the migration energy for one-dimensional motion of a $\langle 111 \rangle$ dumbbell in tungsten was only 2 meV, with the profile of the energy barrier having a simple single peak structure [18]. The transition of a $\langle 111 \rangle$ dumbbell from one equilibrium position to another occurs via a $\langle 111 \rangle$ crowdion configuration as the saddle point. In a classical transition state theory approximation [19] the barrier of 2 meV corresponds to the temperature of the onset of SIA defect migration of 0.7 K, see Section IV below for further detail. A quantum transition theory treatment [18], taking zero-order atomic vibrations into account, predicts that defects would diffuse at even lower temperature. Neither classical nor quantum predictions match experimental observations, and this poses a question about the origin of such a striking disagreement between experimental observations and theoretical predictions based on fairly accurate DFT calculations.

A possible alternative explanation of the observed T_m^{SIA} is that neither a straight $\langle 111 \rangle$ nor a $\langle 110 \rangle$ SIA defect structure is the lowest energy configuration of the defect. For example, Olsson [20] noted that the energy of a $\langle 221 \rangle$ dumbbell configuration in Cr has lower energy than the energy of either $\langle 111 \rangle$ or $\langle 110 \rangle$ configurations, however the matter received no further attention. Han *et al.*[21] also found that the energy of a canted $\langle 111 \rangle$ dumbbell in Mo was slightly lower than that of a straight $\langle 111 \rangle$ dumbbell, although their study gave no detail about how atomic relaxations were performed. Recently, Gharaee and Erhart [22] reported that a lower symmetry interstitial configuration containing Ti, V, or Re in W has lower energy than $\langle 111 \rangle$ and $\langle 110 \rangle$ dumbbell. They called it bridge interstitial. All these studies [20–22] showing a similar effect suggest that there is a more stable SIA configuration in group 6 elements than a simple linear $\langle 111 \rangle$ structure. Provided that a canted dumbbell is the most stable SIA configuration, the migration pathway will not follow the one dimensional diffusion along the $\langle 111 \rangle$ direction.

In this paper, we would like to resolve such a discrepancy between DFT calculations, resistivity recovery experiments, elastic affect effect experiments, and Huang scattering experiments on the structure and migration of SIA in Cr, Mo, and W. We found a canted SIA is the most stable SIA configuration. It adopts a $\langle 11\xi \rangle$ direction, where ξ is a irrational number. We also calculated the migration energy of a $\langle 11\xi \rangle$ dumbbell through a three dimensional translational-rotational migration pathway. Those calculated migration energies of group 6 elements are well compatible with the experimental migration temperatures. We also performed simulation on Huang scattering pattern showing that a $\langle 11\xi \rangle$ dumbbell configuration will generate a pattern resembling a $\langle 110 \rangle$ dumbbell configuration. This explains the origin of all the controversy.

II. METHODOLOGY

All *ab initio* DFT calculations are performed using Vienna Ab initio Simulation Package (VASP)[23–26]. We used the generalized gradient approximation (GGA) exchange-correlation functionals of Perdew-Burke-Ernzerhof (PBE) [27, 28]. Plane wave energy cutoff is 450 eV. A cell size of 4×4×4 BCC unit cells is adopted, where 5×5×5 k-points mesh is used. In order to check the size effect, we performed some simulations on a larger box with 5×5×5 BCC unit cells, where 4×4×4 k-points mesh is used. The volume of perfect lattice simulation cell is relaxed to stress-free condition. Keeping the cell size and shape the same as in the perfect lattice case, we created cells with different SIA configurations, where ionic positions are relaxed. The maximum residue force of an atom is smaller than 1×10^{-3} eV/Å. The semi-core shell is treated as valence electrons. There are 12 valence electron in Cr, Mo and W. It guarantees the the correctness of highly compressed region.

For Mo and W, only non-magnetic (NM) calculations were performed. For Cr, we performed both NM and collinear magnetic calculations. Though the ground state of Cr is believed to be spin density wave (SDW) [29], antiferromagnetic (AFM) state is chosen for spin polarized calculation. AFM state has an energy indistinguishable from SDW within the error of *ab initio* calculations [30]. AFM state is setup through initializing finite magnetic moments similar to perfect lattice case, but with the magnitude of magnetic moments initializing to zero near the core of SIA configuration, followed by self-consistent field calculation.

The formation energy of a defect is defined as:

$$E^F = E_D(N_D) - \frac{N_D}{N_B} E_B(N_B) - E_{el}^{corr}, \qquad (1)$$

where N_B and N_D are the number of atoms in a simulation box of bulk and defect cases, E_D is the total energy of a system with a defect, E_B is the energy of bulk case, and E_{el}^{corr} is the elastic correction energy due to the periodic boundary condition. Details of E_{el}^{corr} can be found in Ref. [12, 31]. Elastic constant tensors are calculated for the computation of E_{el}^{corr}. They are calculated using Le Page and Saxe method [32] using a 2 atoms simulation

PBE	C_{11}	C_{12}	C_{44}	Ω_0	a_0
Cr/AFM	448.12	62.03	102.13	11.72	2.862
Cr/NM	509.67	144.27	105.73	11.49	2.843
Mo	469.07	157.72	99.71	15.77	3.160
W	518.26	199.77	142.09	16.14	3.184
Exp.					
Cr	394.1	88.5	103.75	11.94	2.88
Mo	464.7	161.5	108.9	15.63	3.15
W	522.4	204.4	160.6	15.78	3.16

TABLE I. Elastic constants (GPa) are calculated following Le Page and Saxe[32] method using a 2-atom cell, with 30×30×30 k-point mesh. Atomic volume (Å^3) and lattice constants (Å) are also presented. We performed calculations using GGA-PBE exchange-correlation functionals at non-magnetic (NM) state for Cr, Mo, and W, and at antiferromagnetic (AFM) states for Cr. Experimental values for lattice constants is from Ref. [33], and elastic constants for Cr is from Ref. [34] and for Mo and W are from Ref. [35].

$4\times4\times4$	Cr/AFM	Cr/NM	Mo	W
$\langle 11\xi\rangle$d	6.361	6.074	7.399	10.249
$\langle 111\rangle$d	6.617	6.247	7.475	10.287
$\langle 111\rangle$c	6.555	6.243	7.479	10.289
$\langle 110\rangle$d	6.515	6.218	7.580	10.576
Tetra	6.918	6.889	8.358	11.717
$\langle 100\rangle$d	7.275	7.256	8.890	12.196
Octa	7.354	7.307	8.916	12.265
Vac	3.004	2.875	2.787	3.223
ξ	0.355	0.405	0.468	0.526

TABLE II. The calculated formation energy E^F of point defects in Cr/AFM, Cr/NM, Mo and W. We performed calculations using GGA-PBE exchange-correlation functionals. We used a simulation cell with $4\times4\times4$ BCC unit cells. The $\langle 11\xi\rangle$ dumbbell is the lowest energy configuration amount all SIA configurations. Vacancy data is also supplied for completeness. Unit is in eV. Value of ξ is material dependent.

box with 30×30×30 k-point mesh. Values are shown in Table I.

The migration energy E^M is calculated using the NEB method [36, 37], where E^M is the maximum formation energy change along the transition pathway between two equilibrium configurations. We employed eleven images between two equilibrium configurations. Residual atomic force in each image is less than 0.01 eV/Å. The formation energy of defect in each image due to periodic boundary condition is corrected.

$5\times5\times5$	Cr/AFM	Cr/NM	Mo	W
$\langle 11\xi\rangle$d	6.453	5.919	7.448	10.256
$\langle 111\rangle$d	6.644	6.095	7.519	10.306
$\langle 110\rangle$d	6.548	6.060	7.628	10.579
ξ	0.356	0.397	0.447	0.482

TABLE III. The calculated formation energy E^F of point defects in Cr/AFM, Cr/NM, Mo and W. A simulation cell with $5\times5\times5$ BCC unit cells is used. The $\langle 11\xi\rangle$ dumbbell is still the lowest energy configuration amount all SIA configurations.

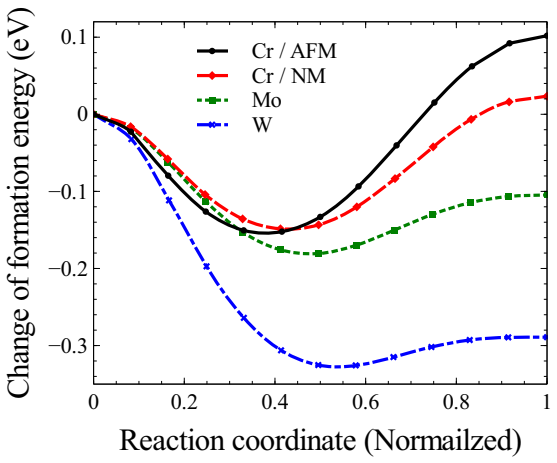

FIG. 2. (Color online) A nudge elastic band calculation of the change of formation energy for a SIA dumbbell rotating from [110] to [111] direction. Elastic correction due to the periodic boundary conditions is imposed.

III. FORMATION ENERGY OF SIA

We performed DFT calculations on various SIA configurations using a simulation cell having $4\times4\times4$ BCC unit cells. They are $\langle 111\rangle$ dumbbell, $\langle 111\rangle$ crowdion, $\langle 110\rangle$ dumbbell, tetrahedral site interstitial, $\langle 100\rangle$ dumbbell, and octahedral site interstitial. For completeness, we also calculated the mono-vacancy case. Their formation energies are presented in Table II. We can see the formation energy of $\langle 110\rangle$ dumbbell, $\langle 111\rangle$ dumbbell and $\langle 111\rangle$ crowdion are fairly close to each other. These values are compatible with previous DFT studies[10, 11, 20, 38] that $\langle 110\rangle$ dumbbell has a lower energy in Cr, and $\langle 111\rangle$ dumbbell has a lower energy in Mo and W.

As inspired by the works by Olsson [20], Han *et al.* [21], and Gharaee and Erhart [22], we speculate that there is a more stable SIA configuration in-between. We performed NEB calculations for a dumbbell rotating from [110] to [111] direction. In Fig. 2, it shows the change of formation energy as a function of reaction coordinate. We can see a clear minimum between [110] and [111] directions in all cases. It is obvious that there is a more stable configuration. We may understand this effect is purely

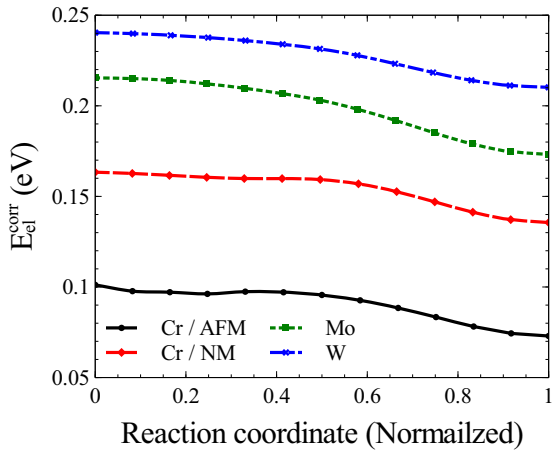

FIG. 3. (Color online) The energy contribution due to the elastic correction E_{el}^{corr} corresponding to Fig. 2.

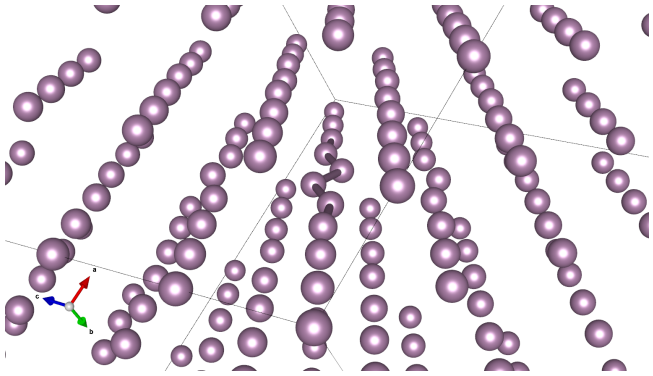

FIG. 4. (Color online) A $\langle 11\xi \rangle$ dumbbell in Mo using a cell with $5 \times 5 \times 5$ unit cells.

chemical. The elastic interaction energy due to the periodic boundary condition E_{el}^{corr}, as shown in Fig. 3, has a contribution that does not affect such conclusion.

In all NEB calculations, we take the lowest energy image, and performed further ionic relaxation. In all cases, they relax to a $\langle 11\xi \rangle$ dumbbell configuration, where their formation energies and the values of ξ are listed in Table II. The $\langle 11\xi \rangle$ dumbbell configuration has the lowest formation energy in all cases. Surprisingly, ξ is an irrational number. It is interesting to note that in the calculation of Cr, both NM and AFM cases prefer a $\langle 11\xi \rangle$ dumbbell configuration. It is different from the case of iron that the most stable $\langle 110 \rangle$ dumbbell configuration is due to magnetism[16].

We checked the size effect by using a larger simulation cell having $5 \times 5 \times 5$ BCC unit cells. We only performed calculations on $\langle 11\xi \rangle$, $\langle 111 \rangle$ and $\langle 110 \rangle$ dumbbells. Their formation energies are presented in Table III. Although the absolute values slightly differ, the conclusion of $\langle 11\xi \rangle$ dumbbell being the most stable SIA configuration remains unchanged. An illustration of the $\langle 11\xi \rangle$ dumbbell in Mo is shown in Fig. 4. For non-cubic cells, we checked the case of $\langle 11\xi \rangle$ dumbbell in Mo using a cell with $4 \times 4 \times 5$ unit cells. Its formation energy is 7.400 eV. It reliefs our concern on the effect of finite size simulation box.

In Fig. 5, we plotted the atomic spacing between two atoms along the $\langle 111 \rangle$ atomic string with an extra atom. They are corresponding to cases of the $\langle 111 \rangle$ dumbbell configuration and $\langle 11\xi \rangle$ dumbbell configuration of Cr/AFM, Cr/NM, Mo and W. We can observe the atomic spacing is slightly larger in the $\langle 11\xi \rangle$ dumbbell configuration for atoms being away from the centre of the SIA configuration. However, the two atoms at the centre of the $\langle 11\xi \rangle$ dumbbell configuration have a distance smaller than the case of $\langle 111 \rangle$ dumbbell configuration.

In Fig. 6, we can see the Voronoi volume of atoms

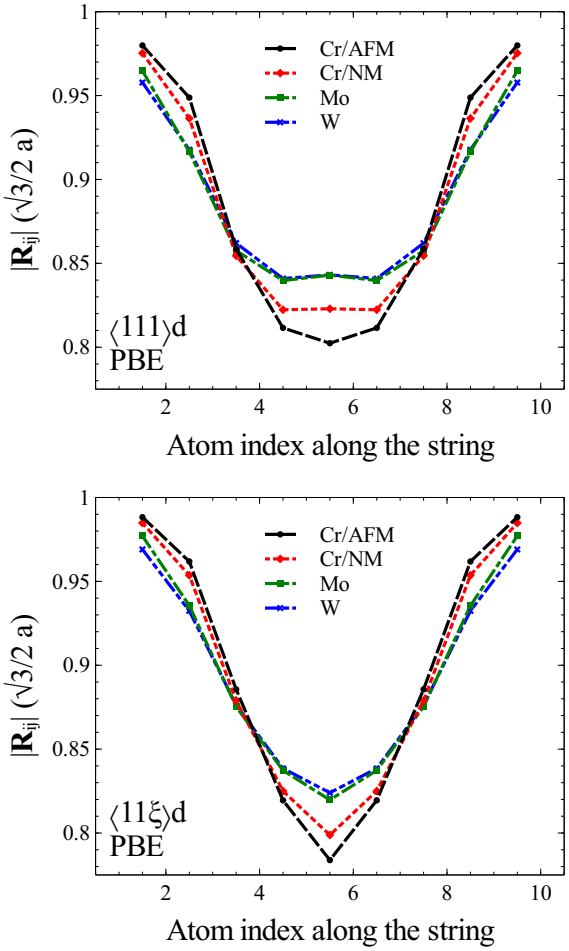

FIG. 5. (Color online) The distance between atom i and $j = i + 1$ along the $\langle 111 \rangle$ string with an extra atom. They are (Top) $\langle 111 \rangle$ dumbbell and (Bottom) $\langle 11\xi \rangle$ configuration of Cr/AFM, Cr/NM, Mo and W. They are all calculated using GGA-PBE functional.

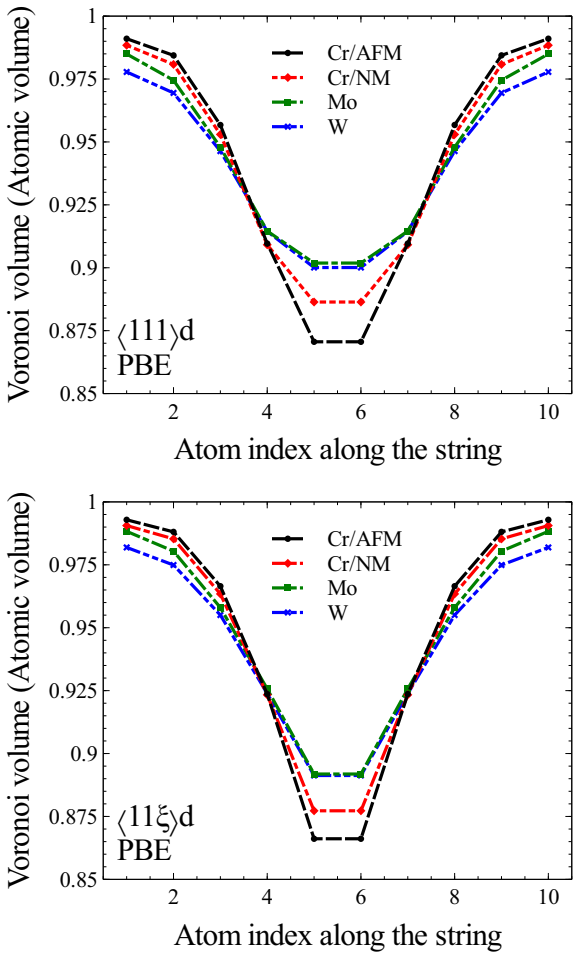

FIG. 6. (Color online) The Voronoi volume of atom i along the $\langle 111\rangle$ string with an extra atom. They are (Top) $\langle 111\rangle$ dumbbell and (Bottom) $\langle 11\xi\rangle$ configuration of Cr/AFM, Cr/NM, Mo and W. They are all calculated using GGA-PBE functional.

along the $\langle 111\rangle$ string. The Voronoi volume is calculated using Voro++[39]. Atoms at the centre of the $\langle 11\xi\rangle$ dumbbell configuration occupy less volume than in $\langle 111\rangle$ dumbbell configuration. However, the Voronoi volume of other atoms along the string is comparatively larger in the case of $\langle 111\rangle$ dumbbell configuration. Data on Voronoi volume is compatible with atomic spacing. The $\langle 11\xi\rangle$ dumbbell configuration appears to be a more localized configuration, and is more profound in the Cr case.

We may analyses such phenomenon a bit further by looking at the difference electron density map. The difference electron density equals the electron density minus the superposition of atomic charge density. The difference electron density for the $\langle 11\xi\rangle$ dumbbell configuration is plotted in Fig. 7. It appears that the two atoms at the centre are buckling away from a $\langle 111\rangle$ string. In Fig, 8, we also plotted the difference electron density for $\langle 111\rangle$ dumbbell configuration. A main difference is that electrons concentrate along the $\langle 111\rangle$ string in the case

Metal	E^m (eV)	est. T_m (K)	exp. T_m (K)
Cr/AFM	0.052	18.7	40
Cr/NM	0.075	27.0	40
Mo	0.064	23.5	35
W	0.040	14.7	27

TABLE IV. The calculated migration energy, the estimated migration temperature, and the migration temperature obtained from electron irradiated resistivity recovery experiment[14]. The estimated T_m is calculated according to the classical transition state theory.

of $\langle 111\rangle$ dumbbell configuration. In the case of $\langle 11\xi\rangle$ dumbbell configuration, it forms a network-like bonding. It may be a viable way of achieving lower energy, and help relaxing the stresses along the atomic string.

IV. MIGRATION ENERGY OF SIA

An important implication of the $\langle 11\xi\rangle$ dumbbell configuration is that the SIA in group 6 elements does not migration through a one dimensional diffusion. It means we need to find a new explanation other than the one suggested by Fitzgerald and Nguyen-Manh[17] assuming $\langle 111\rangle$ dumbbell configuration being the most stable SIA configuration, and migrate through the $\langle 111\rangle$ direction.

If we look at the case of magnetic iron, it adopts a $\langle 110\rangle$ dumbbell configuration. The SIA migrates through a three dimensional translational rotational pathway. DFT calculation suggests a SIA migrates from a [110] dumbbell to the adjacent [011] dumbbell configuration having a migration barrier of 0.34 eV [16]. It is compatible with a relatively high experimental verified migration temperature of 120K or a migration energy of 0.30eV [14].

Since experimental data for the migration temperature of SIA in Cr, Mo and W are 40K, 35K and 27K[14], respectively, we speculate the SIA migrates through a translational rotational pathway similar to Fe. A $\langle 11\xi\rangle$ dumbbell is in between the $\langle 111\rangle$ and $\langle 110\rangle$ directions. A possible migration pathway would be from [11ξ] to adjacent [ξ11]. Due to symmetry, a [11ξ] dumbbell can also jump to [1ξ1] position. For any $\langle 11\xi\rangle$ dumbbell, there are two equivalent forward and two backward migration pathways along the $\langle 111\rangle$ direction. A schematic picture is shown in Fig. 9.

Such a migration pathway does not induce large non-elastic relaxation, it is compatible with the elastic affect effect experiment on Mo at 4.2K [13]. Although there is reorientation of the SIA direction during migration, it is relatively small if one compares it with the translational-rotational migration of $\langle 110\rangle$ SIA in Fe. Besides, though its migration pathway is not unique, the migration of a $\langle 11\xi\rangle$ dumbbell is essentially on the 110 plane and along $\langle 111\rangle$ direction, which is the same as the two dimensional diffusion as suggested by Jacques and Robrock [13] show-

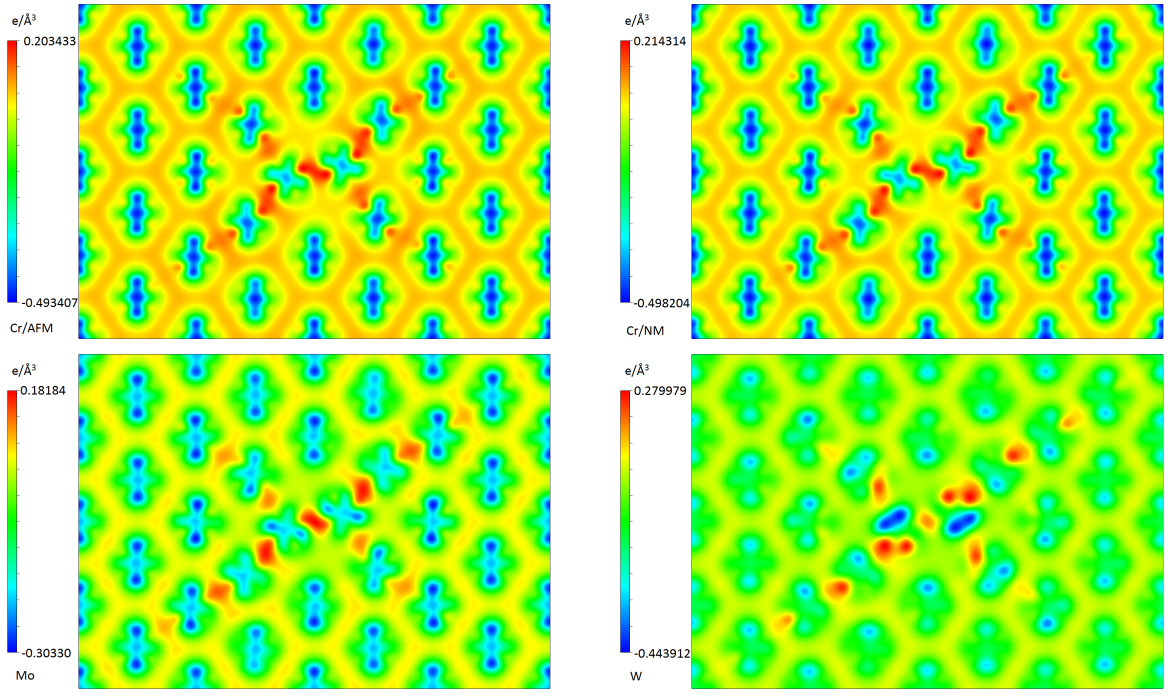

FIG. 7. (Color online) A two dimensional plot of the difference electron density of a $\langle 11\xi \rangle$ dumbbell configuration on a $(1\bar{1}0)$ plane for the Cr/AFM, Cr/NM, Mo and W calculated using GGA-PBE functional. The difference electron density equals the electron density minus the superposition of atomic charge density.

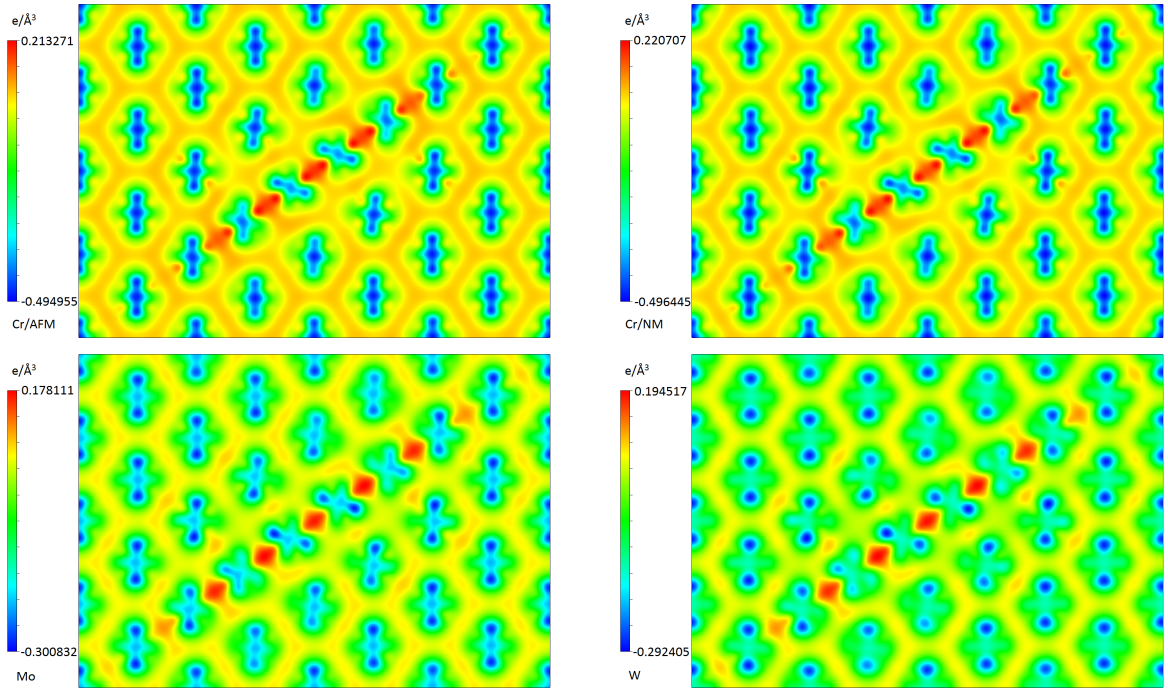

FIG. 8. (Color online) A two dimensional plot of the difference electron density of a $\langle 111 \rangle$ dumbbell configuration on a $(1\bar{1}0)$ plane for the Cr/AFM, Cr/NM, Mo and W calculated using GGA-PBE functional.

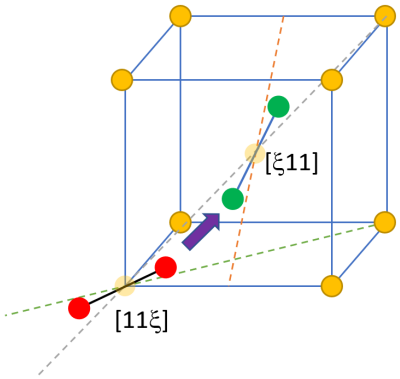

FIG. 9. Schematic picture on the migration of an SIA from [11ξ] to [ξ11] dumbbell configuration. The values of ξ for Group 6 elements are listed in Table II and III.

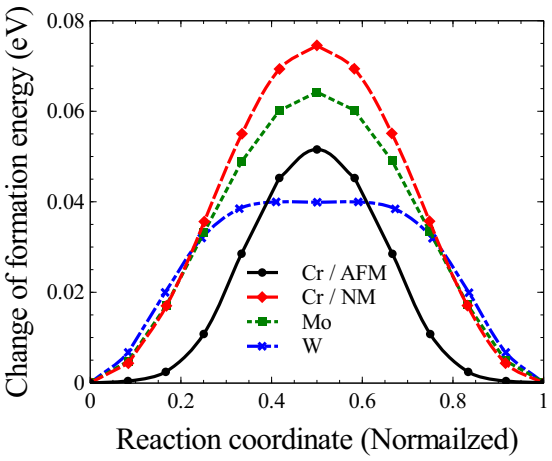

FIG. 10. (Color online) A nudge elastic band calculation for a [11ξ] dumbbell migrating to adjacent [ξ11] dumbbell configuration. We performed calculations using GGA-PBE exchange-correlation functionals.

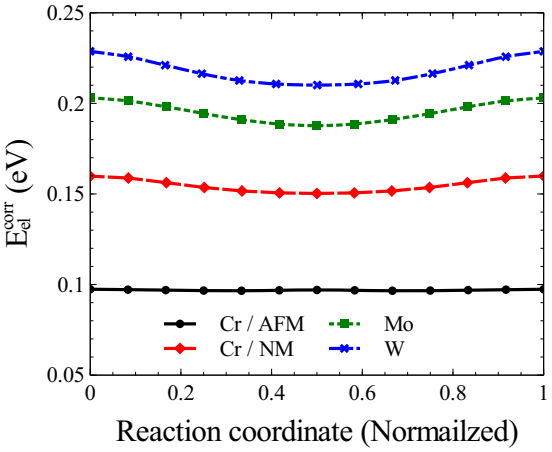

FIG. 11. (Color online) The energy contribution due to the elastic correction E_{el}^{corr} corresponding to Fig. 10.

ing in Fig. 1.

NEB calculation for the migration of an SIA from [11ξ] to [ξ11] dumbbell configuration were performed. The change of formation energy as a function of reaction coordinate is shown in Fig. 10. The corresponding values of E_{int} is shown in Fig. 11. The migration energy is taken as the difference of energy between the equilibrium and saddle point. As presented in Table IV, the migration energy of Cr/AFM is 0.052eV, Cr/NM is 0.075eV, Mo is 0.064 eV and W is 0.040eV.

If we assume the jump frequency can be described by the classical transition state theory[19], the jump frequency can be written as

$$\nu = \nu_0 \exp(-E^m/k_B T), \tag{2}$$

where ν_0 is the attempt frequency. We may approximate the attempt frequency by the Debye frequency according to the Debye temperature θ.

Using Fe as a benchmark, if we assume $\nu = 1\text{s}^{-1}$, where $\theta_{\text{Fe}} = 470\text{K}$ [33], one can obtain a $T_m = 124.3\text{K}$ according to the migration energy of a ⟨110⟩ dumbbell in Fe with $E^m = 0.34\text{eV}$ [16]. It is well compatible with the migration temperature of SIA being 120K according to experiment [14].

Similarly, using the Debye temperature $\theta_{\text{Cr}} = 630\text{K}$, $\theta_{\text{Mo}} = 450\text{K}$ and $\theta_{\text{W}} = 400\text{K}$ (Ref. [33]), we can estimate the corresponding T_m^{SIA} being 18.7K, 27.0K, 23.5K, and 14.7K for Cr/AFM, Cr/NM, Mo and W, respectively. They are well compatible with electron irradiated resistivity recovery experiments that the SIA T_m^{SIA} are at 40K, 35, 27K for Cr, Mo and W [14]. Provided that the migration barrier of SIA in W is only 2meV[18], the estimated migration temperature is 0.7K, which is too low comparing to experiment.

For higher temperature cases, we cannot ignore the possibility of a two-step migration mechanism. A ⟨11ξ⟩ dumbbell may rotate to a ⟨111⟩ dumbbell, followed by one dimensional diffusion. If we observe the difference of formation energies between a ⟨11ξ⟩ and a ⟨111⟩ SIA in Mo and W, they are 0.071eV and 0.050, which are not much higher than the migration energy of a SIA through a [11ξ] to [ξ11] pathway.

V. HUANG SCATTERING PATTERN

In previous sections, we discussed the equilibrium configuration of an SIA in Cr, Mo, and W, and its translational-rotational but pseudo-one-dimensional migration pathway along the ⟨111⟩ direction. It resolved the controversy between DFT, resistivity recovery experiments and elastic affect effect experiments. Finally, we are going to simulate the Huang scattering pattern using the DFT data that we just calculated. It will complete our investigation.

Assuming a small concentration of statically distributed point defects, the symmetry of its long range

Cr/AFM	P_{11}	P_{22}	P_{33}	P_{12}	P_{23}	P_{31}	π_1	π_2	π_3	π_2/π_1	π_3/π_1
$\langle 11\xi\rangle$d	18.389	18.389	21.882	4.040	2.058	2.058	1147.0	4.067	16.528	0.00355	0.01441
$\langle 111\rangle$d	18.728	18.728	18.728	4.617	4.617	4.617	1052.2	0.000	42.635	0.00000	0.04052
$\langle 110\rangle$d	20.530	20.530	18.955	4.790	0.000	0.000	1200.6	0.827	15.299	0.00069	0.01274

TABLE V. The dipole tensors P_{ij} (in unit eV) and π_1, π_2, and π_3 of $\langle 11\xi\rangle$, $\langle 111\rangle$, and $\langle 110\rangle$ dumbbell in Cr/AFM. They are calculated using a $4\times4\times4$ unit cells.

Cr/NM	P_{11}	P_{22}	P_{33}	P_{12}	P_{23}	P_{31}	π_1	π_2	π_3	π_2/π_1	π_3/π_1
$\langle 11\xi\rangle$d	27.410	27.410	32.365	4.417	2.662	2.662	2533.8	8.181	22.455	0.00323	0.00886
$\langle 111\rangle$d	28.816	28.816	28.816	5.222	5.222	5.222	2491.0	0.000	54.543	0.00000	0.02190
$\langle 110\rangle$d	28.806	28.806	30.494	4.594	0.000	0.000	2587.6	0.950	14.071	0.00037	0.00544

TABLE VI. The dipole tensors P_{ij} (in unit eV) and π_1, π_2, and π_3 of $\langle 11\xi\rangle$, $\langle 111\rangle$, and $\langle 110\rangle$ dumbbell in Cr/NM. They are calculated using a $4\times4\times4$ unit cells.

strain field can be determined by Huang scattering. The average of Huang intensities over all possible orientations of a defect for a momentum transfer $\mathbf{K}=\mathbf{h}+\mathbf{q}$ can be written as [8],

$$S_H(\mathbf{K}) = N_{def} f_{\mathbf{h}}^2 \frac{h^2}{q^2}\frac{1}{V_{uc}^2}\left(\gamma_1\pi_1+\gamma_2\pi_2+\gamma_3\pi_3\right) \tag{3}$$

where N_{def} is the number of defect, $f_{\mathbf{h}}$ is atomic form factor, $V_{uc}=a_0^3$ is the volume of unit cell, $\mathbf{h}$ is a reciprocal lattice vector, $\mathbf{q}$ measures the deviation from the Bragg reflection, where $\mathbf{q}$ is small comparing to $\mathbf{h}$. γ_1, γ_2, and γ_3 depends on $\mathbf{h}$ and $\mathbf{q}$, and also the anisotropic elastic constants, where

$$\gamma_1 = \frac{1}{3}\left(\sum_i T_{ii}\right)^2, \tag{4}$$

$$\gamma_2 = \frac{1}{3}\sum_{i>j}\left(T_{ii}-T_{jj}\right)^2, \tag{5}$$

$$\gamma_3 = \frac{1}{2}\sum_{i>j}\left(T_{ij}+T_{ji}\right)^2, \tag{6}$$

and

$$T_{ij} = \sum_l \hat{h}_l g_{li}(\hat{\mathbf{q}})\hat{q}_j. \tag{7}$$

The unit vectors $\hat{\mathbf{h}}=\mathbf{h}/h$ and $\hat{\mathbf{q}}=\mathbf{q}/q$. The matrix function

$$g_{ij}(\hat{\mathbf{q}}) = \left(\sum_{kl} C_{ikjl}\hat{q}_k\hat{q}_l\right)^{-1}. \tag{8}$$

where C_{ijkl} is elastic constant tensor. π_1, π_2, and π_3 depends only on the elastic dipole tensor P_{ij} of a defect in *one* particular orientation, where

$$\pi_1 = \frac{1}{3}\left(\sum_i P_{ii}\right)^2, \tag{9}$$

$$\pi_2 = \frac{1}{6}\sum_{i>j}\left(P_{ii}-P_{jj}\right)^2, \tag{10}$$

$$\pi_3 = \frac{2}{3}\sum_{i>j} P_{ij}^2. \tag{11}$$

Due to the symmetry of π_1, π_2, and π_3 , any degenerated orientation of a defect will give the same values.

In our previous works [12, 31], we presented the method of obtaining the dipole tensor of any localized defect from *ab initio* calculation. The dipole tensor of a localized defect can be calculated from macro-stresses developing in a simulation box due to the presence of a defect [31, 40–42],

$$P_{ij} = V_{cell}(C_{ijkl}\epsilon_{kl}^{app} - \bar{\sigma}_{ij}), \tag{12}$$

where

$$\bar{\sigma}_{ij} = \frac{1}{V_{cell}}\int_{V_{cell}}\sigma_{ij}dV \tag{13}$$

is the average macroscopic stress in the simulation box, and ϵ_{kl}^{app} is external applied stresses. In current work, since we are using simulation boxes of the same size and shape as in perfect lattice case, it means $\epsilon_{kl}^{app}=0$. The value of P_{ij} of Cr/AFM, Cr/NM, Mo and W are presented in Table V to VIII. Calculated values of π_1, π_2, and π_3 are also presented.

The atomic form factor may be approximated by a sum of Gaussian functions of the form [43]:

$$f_{\boldsymbol{\kappa}} = \sum_{i=1}^{4} a_i \exp\left(-b_i\left(\frac{\kappa}{4\pi}\right)\right) + c, \tag{14}$$

where a_i, b_i and c for Cr, Mo and W are listed in Table IX. The atomic form factor can be treated as a constant for particular reflection in the case of Huang scattering.

In Fig. 12 to 15, we present simulated Huang scattering pattern for $\langle 100\rangle$, $\langle 111\rangle$, $\langle 110\rangle$, and $\langle 11\xi\rangle$ dumbbells

Mo	P_{11}	P_{22}	P_{33}	P_{12}	P_{23}	P_{31}	π_1	π_2	π_3	π_2/π_1	π_3/π_1
$\langle 11\xi\rangle$d	38.614	38.614	43.538	6.675	4.631	4.631	4861.4	8.082	58.301	0.00166	0.01441
$\langle 111\rangle$d	39.601	39.601	39.601	7.609	7.609	7.609	4704.6	0.000	115.789	0.00000	0.04052
$\langle 110\rangle$d	39.944	39.944	42.470	6.757	0.000	0.000	4990.4	2.128	30.438	0.00043	0.01274
Exp.										0.05±0.02	0.04± 0.02

TABLE VII. The dipole tensors P_{ij} (in unit eV) and π_1, π_2, and π_3 of $\langle 11\xi\rangle$, $\langle 111\rangle$, and $\langle 110\rangle$ dumbbell in Mo. They are calculated using a $4\times4\times4$ unit cells. Experimental results is taken from Ehrhart [9] with sample being put under electron irradiation.

W	P_{11}	P_{22}	P_{33}	P_{12}	P_{23}	P_{31}	π_1	π_2	π_3	π_2/π_1	π_3/π_1
$\langle 11\xi\rangle$d	50.921	50.921	57.883	11.925	9.136	9.136	8503.9	16.157	206.078	0.00190	0.01441
$\langle 111\rangle$d	52.754	52.754	52.754	13.128	13.128	13.128	8348.9	0.000	344.712	0.00000	0.04052
$\langle 110\rangle$d	52.557	52.557	56.960	11.277	0.000	0.000	8756.0	6.462	84.777	0.00074	0.01274

TABLE VIII. The dipole tensors P_{ij} (in unit eV) and π_1, π_2, and π_3 of $\langle 11\xi\rangle$, $\langle 111\rangle$, and $\langle 110\rangle$ dumbbell in W. They are calculated using a $4\times4\times4$ unit cells.

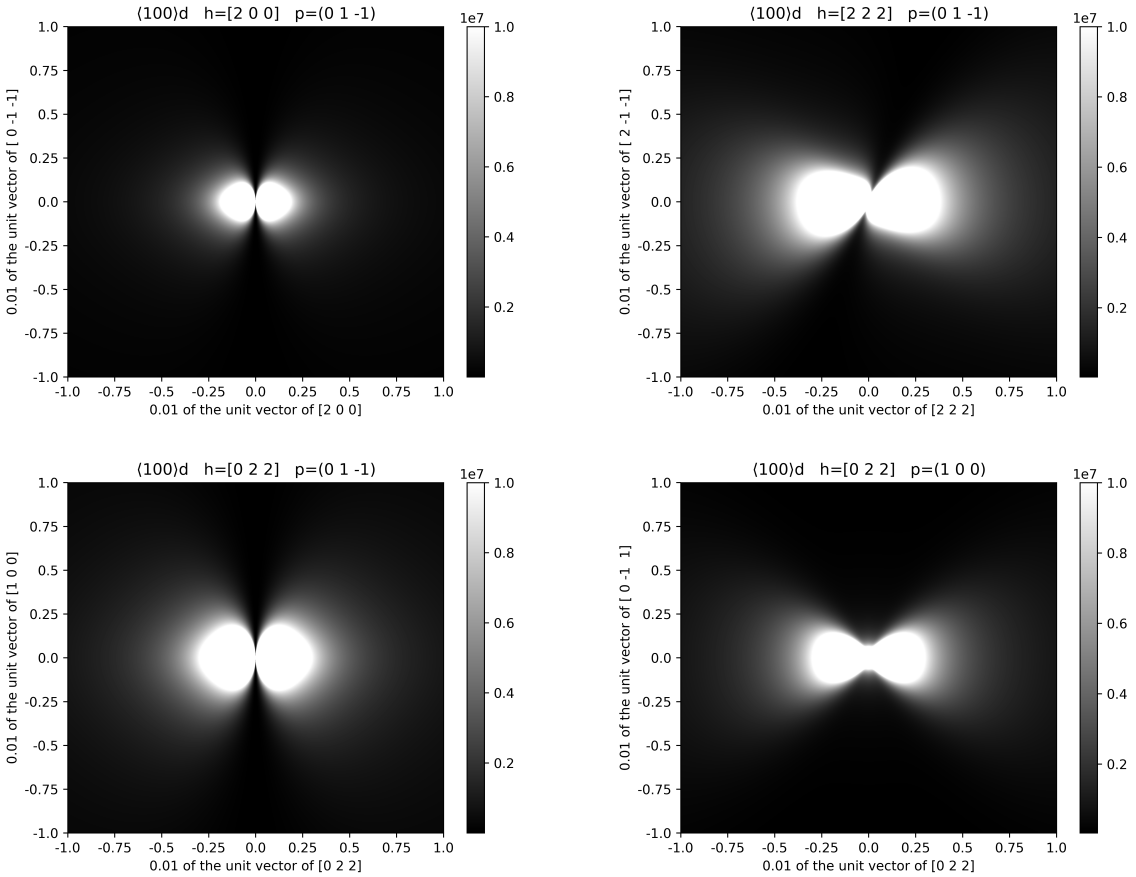

FIG. 12. Simulated Huang scattering pattern for $\langle 100\rangle$ dumbbell configuration for a **h** reflection in the **p** plane. **h** is the reciprocal lattice vector. **q** is in the reciprocal plane **p**.

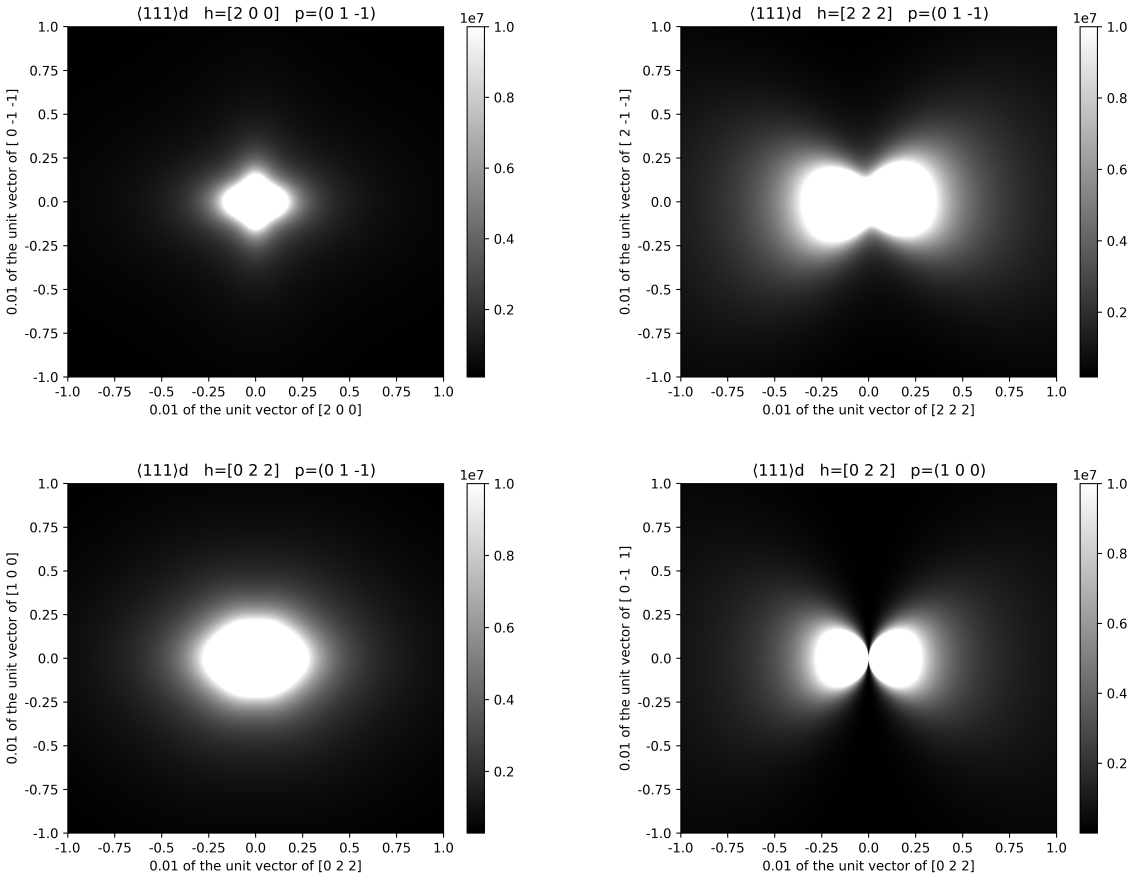

FIG. 13. Simulated Huang scattering pattern for ⟨111⟩ dumbbell configuration for a **h** reflection in the **p** plane. **h** is the reciprocal lattice vector. **q** is in the reciprocal plane **p**.

Element	a_1	b_1	a_2	b_2	a_3	b_3	a_4	b_4	c
Cr	10.6406	6.1038	7.3537	0.392	3.324	20.2626	1.4922	98.7399	1.1832
Mo	3.7025	0.2772	17.2356	1.0958	12.8876	11.004	3.7429	61.6584	4.3875
W	29.0818	1.72029	15.43	9.2259	14.4327	0.321703	5.11982	57.056	9.8875

TABLE IX. The parameters for calculating the atomic form factor according to Ref. [43].

in Mo. We put $N_{def} = 1$ for all calculations. It essentially means the calculated intensity is in unit of per defect. Since $S_H(\mathbf{K})$ diverges at $q = 0$, we impose a maximum cutoff value of 1×10^7 on the plotted intensity. We take the value of **h** and **q** according to the criteria for distinguishing different SIAs as discussed by Dederichs [8] and Ehrhart [9]. We take **h**=[200], [222] and [022], and **q** being in the plane $\mathbf{p} = (01\bar{1})$ of reciprocal lattice. We also take $\mathbf{h} = [022]$ and $\mathbf{p} = (100)$.

In the case of ⟨100⟩ dumbbell, we can see zero intensity line for $\mathbf{h} = [200]$ & $\mathbf{p} = (01\bar{1})$ and $\mathbf{h} = [022]$ & $\mathbf{p} = (01\bar{1})$. In the case of ⟨111⟩ dumbbell, only $\mathbf{h} = [022]$ & $\mathbf{p} = (100)$ shows zero intensity line. In the case of ⟨110⟩ and ⟨11ξ⟩ dumbbell, none of them show zero intensity line. In Fig. 16, we show the Huang scattering pattern with a smaller value range of **q** for better observation of the zero intensity line. All patterns corresponding to ⟨100⟩, ⟨111⟩, ⟨110⟩ dumbbell are compatible with calculations by Dederichs [8] and Ehrhart [9].

The major limitation in the analysis by Ehrhart [9] is the assumption that only ⟨100⟩, ⟨111⟩, ⟨110⟩ dumbbell are candidates of the configuration of SIA. According to our simulated Huang scattering pattern, we found that one cannot distinguish the patterns corresponding to the ⟨110⟩ and ⟨11ξ⟩ dumbbell. It means that the detection of ⟨11ξ⟩ dumbbell SIA may be misinterpreted as the ⟨110⟩ dumbbell. Indeed, if we look at the construction of π_1, π_2 and π_3, they are all non-zero for both ⟨110⟩ and ⟨11ξ⟩ dumbbell cases, which is the reason that Huang scattering experiment cannot distinguish these two SIA config-

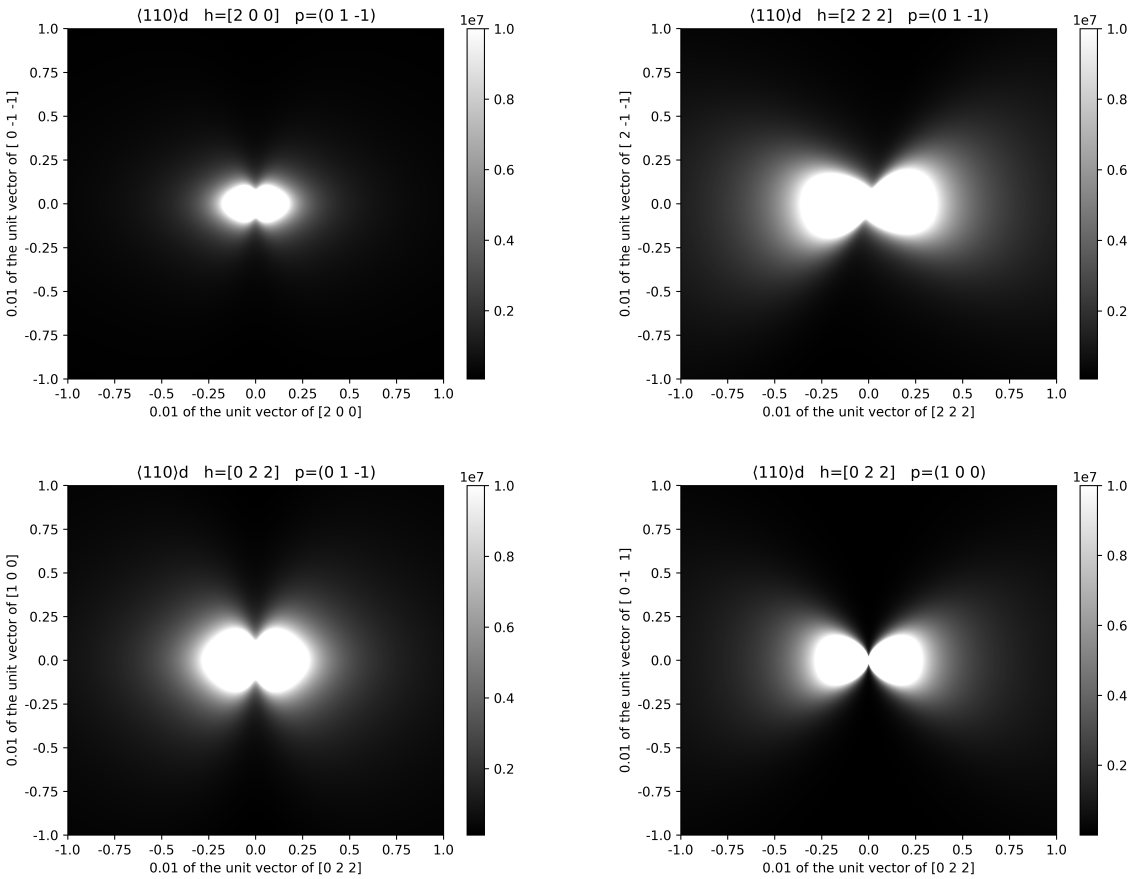

FIG. 14. Simulated Huang scattering pattern for ⟨110⟩ dumbbell configuration for a **h** reflection in the **p** plane. **h** is the reciprocal lattice vector. **q** is in the reciprocal plane **p**.

urations.

VI. CONCLUSION

We found that a low symmetry canted dumbbell configuration having the lowest formation energy amount other SIA configurations in Cr, Mo and W. It adopts a $\langle 11\xi \rangle$ dumbbell configuration, where ξ is an irrational number. The value of ξ is material dependent. We have been checking the size effect using a larger simulation box with $5\times5\times5$ BCC unit cells and a rectangular simulation box. It leads to the same conclusion. A three dimensional translational rotational, but pseudo-one-dimensional migration pathway is suggested. Nudge elastic band calculations were performed. The energy required for a $[11\xi]$ dumbbell to migrate to adjacent $[\xi11]$ dumbbell configuration in Cr/AFM is 0.052eV, Cr/NM is 0.075eV, Mo is 0.064 eV and W is 0.040eV. The corresponding estimated migration temperatures are well compatible with experimental values. We also simulated the Huang scattering pattern showing that $\langle 110 \rangle$ and $\langle 11\xi \rangle$ dumbbell are indistinguishable. It resolves the discrepancy between DFT calculation, the resistive recovery experiment, elastic affect effect experiment and Huang scattering experiment on the structural of SIA and long range SIA migration temperature of group 6 elements.

ACKNOWLEDGMENTS

We would like to thank Pär Olsson for fruitful discussion. This work has been carried out within the framework of the EUROfusion Consortium and has received funding from the Euratom research and training programme 2014-2018 and 2019-2020 under grant agreement No. 633053 and from the RCUK Energy Programme [grant number EP/P012450/1]. To obtain further information on the data and models underlying this paper please contact PublicationsManager@ukaea.uk. The views and opinions expressed herein do not necessarily reflect those of the European Commission. We also acknowledge EUROFusion for the provision of access to Marconi supercomputer facility at CINECA in Italy.

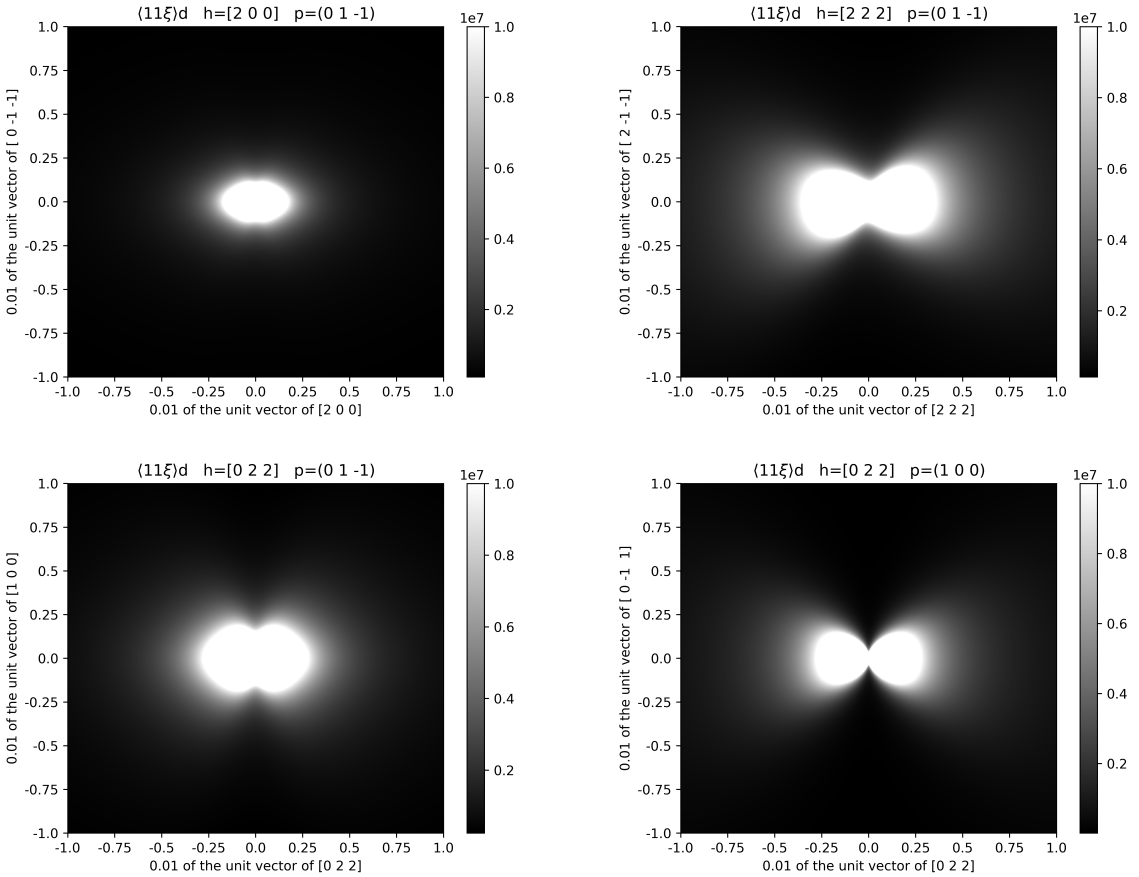

FIG. 15. Simulated Huang scattering pattern for $\langle 11\xi \rangle$ dumbbell configuration for a **h** reflection in the **p** plane. **h** is the reciprocal lattice vector. **q** is in the reciprocal plane **p**.

[1] E.A. Little and D.A. Stow, "Void-swelling in irons and ferritic steels: Ii. an experimental survey of materials irradiated in a fast reactor," Journal of Nuclear Materials **87**, 25 – 39 (1979).

[2] V. K. Kharchenko and V. V. Bukhanovskii, "High-temperature strength of refractory metals, alloys and composite materials based on them. part 1. tungsten, its alloys, and composites," Strength of Materials **44**, 512–517 (2012).

[3] V. K. Kharchenko and V. V. Bukhanovskii, "High-temperature strength of refractory metals, alloys and composite materials based on them. part 2. molybdenum and niobium alloys," Strength of Materials **44**, 617–625 (2012).

[4] Dong Yong Park, Yong Jun Oh, Young Sam Kwon, Seong Taek Lim, and Seong Jin Park, "Development of non-eroding rocket nozzle throat for ultra-high temperature environment," International Journal of Refractory Metals and Hard Materials **42**, 205 – 214 (2014).

[5] Derek Stork, Pietro Agostini, Jean-Louis Boutard, Derek Buckthorpe, Eberhard Diegele, Sergei L. Dudarev, Colin English, Gianfranco Federici, Mark R. Gilbert, Sehila Gonzalez, Angel Ibarra, Christian Linsmeier, Antonella Li Puma, Gabriel Marbach, Lee W. Packer, Baldev Raj, Michael Rieth, Min Quang Tran, David J. Ward, and Steven J. Zinkle, "Materials r&d for a timely demo: Key findings and recommendations of the eu roadmap materials assessment group," Fusion Engineering and Design **89**, 1586 – 1594 (2014), proceedings of the 11th International Symposium on Fusion Nuclear Technology-11 (ISFNT-11) Barcelona, Spain, 15-20 September, 2013.

[6] D. Stork, P. Agostini, J.L. Boutard, D. Buckthorpe, E. Diegele, S.L. Dudarev, C. English, G. Federici, M.R. Gilbert, S. Gonzalez, A. Ibarra, Ch. Linsmeier, A. Li Puma, G. Marbach, P.F. Morris, L.W. Packer, B. Raj, M. Rieth, M.Q. Tran, D.J. Ward, and S.J. Zinkle, "Developing structural, high-heat flux and plasma facing materials for a near-term demo fusion power plant: The eu assessment," Journal of Nuclear Materials **455**, 277 – 291 (2014), proceedings of the 16th International Conference on Fusion Reactor Materials (ICFRM-16).

[7] M. Durrand-Charre, *Microstructure of Steels and Cast Irons* (Springer-Verlag, Berlin, 2003).

[8] P. H. Dederichs, "The theory of diffuse x-ray scattering and its application to the study of point defects and

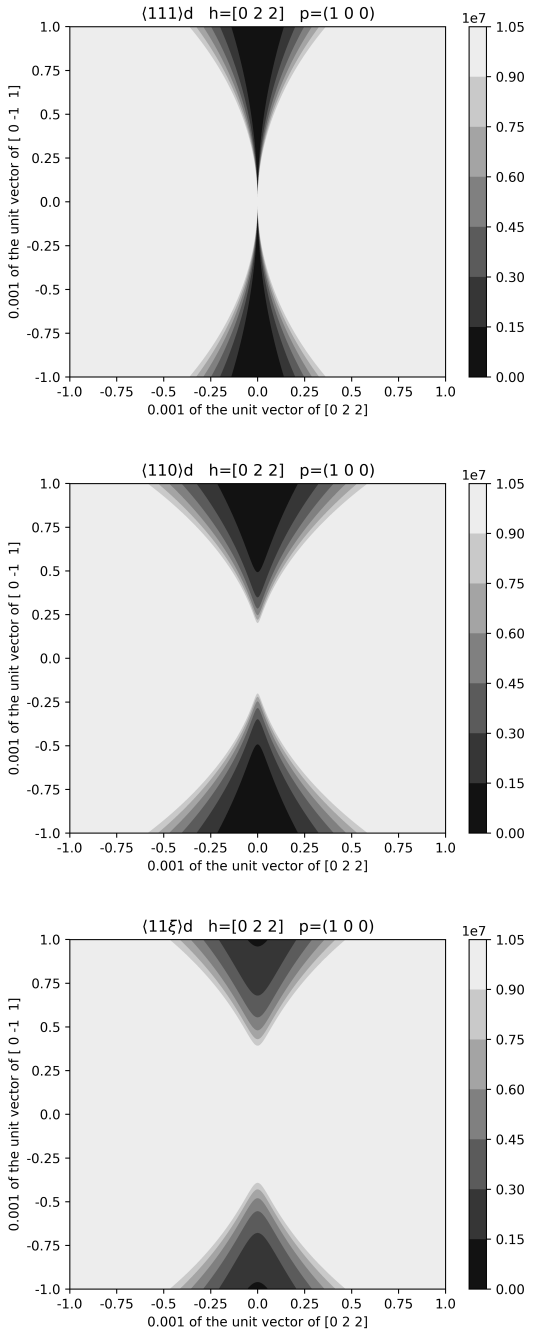

FIG. 16. Simulated Huang scattering pattern for ⟨111⟩, ⟨110⟩ and ⟨11ξ⟩ dumbbell configurations for a [022] reflection in the (100) plane. Parallel to the $[0\bar{1}1]$ direction, only ⟨111⟩ dumbbell configuration shows zero intensity line.

their clusters," Journal of Physics F: Metal Physics **3**, 471 (1973).

[9] P. Ehrhart, "The configuration of atomic defects as determined from scattering studies," Journal of Nuclear Materials **69-70**, 200 – 214 (1978).

[10] P. M. Derlet, D. Nguyen-Manh, and S. L. Dudarev, "Multiscale modeling of crowdion and vacancy defects in body-centered-cubic transition metals," Phys. Rev. B **76**, 054107 (2007).

[11] D. Nguyen-Manh, A. P. Horsfield, and S. L. Dudarev, "Self-interstitial atom defects in bcc transition metals: Group-specific trends," Phys. Rev. B **73**, 020101 (2006).

[12] Pui-Wai Ma and S. L. Dudarev, "The universality of point defect structure in body-centred cubic metals," Physical Review Materials (2018).

[13] Jacques, H. and Robrock, K.-H., "Elastic after effect studies of molybdenum after electron irradiation at 4.7 k," J. Phys. Colloques **42**, 723 – 728 (1981).

[14] P. Ehrhart, P. Jung, H. Schultz, and H. Ullmaier, *Landolt-Börnstein - Group III Condensed Matter · Volume 25: "Atomic Defects in Metals"*, edited by H. Ullmaier (Springer-Verlag Berlin Heidelberg, 1991).

[15] H. Schultz, "Defect parameters of b.c.c. metals: group-specific trends," Materials Science and Engineering: A **141**, 149 – 167 (1991).

[16] Chu-Chun Fu, F. Willaime, and P. Ordejón, "Stability and mobility of mono- and di-interstitials in α-fe," Phys. Rev. Lett. **92**, 175503 (2004).

[17] S. P. Fitzgerald and D. Nguyen-Manh, "Peierls potential for crowdions in the bcc transition metals," Phys. Rev. Lett. **101**, 115504 (2008).

[18] Thomas D. Swinburne, Pui-Wai Ma, and Sergei L. Dudarev, "Low temperature diffusivity of self-interstitial defects in tungsten," New Journal of Physics **19**, 073024 (2017).

[19] George H. Vineyard, "Frequency factors and isotope effects in solid state rate processes," Journal of Physics and Chemistry of Solids **3**, 121 – 127 (1957).

[20] P. Olsson, "Ab initio study of interstitial migration in fecr alloys," Journal of Nuclear Materials **386-388**, 86 – 89 (2009), fusion Reactor Materials.

[21] Seungwu Han, Luis A. Zepeda-Ruiz, Graeme J. Ackland, Roberto Car, and David J. Srolovitz, "Self-interstitials in v and mo," Phys. Rev. B **66**, 220101 (2002).

[22] Leili Gharaee and Paul Erhart, "A first-principles investigation of interstitial defects in dilute tungsten alloys," Journal of Nuclear Materials **467**, 448 – 456 (2015).

[23] G. Kresse and J. Hafner, "Ab initio molecular dynamics for liquid metals," Phys. Rev. B **47**, 558–561 (1993).

[24] G. Kresse and J. Hafner, "Ab initio molecular-dynamics simulation of the liquid-metal–amorphous-semiconductor transition in germanium," Phys. Rev. B **49**, 14251–14269 (1994).

[25] G. Kresse and J. Furthmüller, "Efficiency of ab-initio total energy calculations for metals and semiconductors using a plane-wave basis set," Computational Materials Science **6**, 15 – 50 (1996).

[26] G. Kresse and J. Furthmüller, "Efficient iterative schemes for ab initio total-energy calculations using a plane-wave basis set," Phys. Rev. B **54**, 11169–11186 (1996).

[27] John P. Perdew, Kieron Burke, and Matthias Ernzerhof, "Generalized gradient approximation made simple," Phys. Rev. Lett. **77**, 3865–3868 (1996).

[28] John P. Perdew, Kieron Burke, and Matthias Ernzerhof, "Generalized gradient approximation made simple [phys. rev. lett. 77, 3865 (1996)]," Phys. Rev. Lett. **78**, 1396–1396 (1997).

[29] R. Hafner, D. Spišák, R. Lorenz, and J. Hafner, "Magnetic ground state of cr in density-functional theory," Phys. Rev. B **65**, 184432 (2002).

[30] S. Cottenier, B. De Vries, J. Meersschaut, and M. Rots, "What density-functional theory can tell us about the spin-density wave in cr," Journal of Physics: Condensed Matter **14**, 3275 (2002).

[31] S. L. Dudarev and Pui-Wai Ma, "Elastic fields, dipole tensors, and interaction between self-interstitial atom defects in bcc transition metals," Phys. Rev. Materials **2**, 033602 (2018).

[32] Yvon Le Page and Paul Saxe, "Symmetry-general least-squares extraction of elastic data for strained materials from ab initio calculations of stress," Phys. Rev. B **65**, 104104 (2002).

[33] Charles Kittel, *Introduction to Solid State Physics*, 8th ed. (John Wiley & Sons, Inc., New York, 2004).

[34] S. B. Palmer and E. W. Lee, "The elastic constants of chromium," The Philosophical Magazine: A Journal of Theoretical Experimental and Applied Physics **24**, 311–318 (1971).

[35] M. W. Finnis and J. E. Sinclair, "A simple empirical n-body potential for transition metals," Philosophical Magazine A **50**, 45–55 (1984).

[36] Gregory Mills, Hannes Jnsson, and Gregory K. Schenter, "Reversible work transition state theory: application to dissociative adsorption of hydrogen," Surface Science **324**, 305 – 337 (1995).

[37] Hannes Jónsson, Greg Mills, and Karsten W. Jacobsen, "Nudged elastic band method for finding minimum energy paths of transitions," in *Classical and Quantum Dynamics in Condensed Phase Simulations* (World Scientific, 1998) pp. 385–404.

[38] Pär Olsson, Christophe Domain, and Janne Wallenius, "Ab initio study of cr interactions with point defects in bcc fe," Phys. Rev. B **75**, 014110 (2007).

[39] Chris H. Rycroft, "Voro++: A three-dimensional voronoi cell library in c++," Chaos: An Interdisciplinary Journal of Nonlinear Science **19**, 041111 (2009).

[40] Emmanuel Clouet, Sbastien Garruchet, Hoang Nguyen, Michel Perez, and Charlotte S. Becquart, "Dislocation interaction with c in α-fe: A comparison between atomic simulations and elasticity theory," Acta Materialia **56**, 3450 – 3460 (2008).

[41] Céline Varvenne, Fabien Bruneval, Mihai-Cosmin Marinica, and Emmanuel Clouet, "Point defect modeling in materials: Coupling ab initio and elasticity approaches," Phys. Rev. B **88**, 134102 (2013).

[42] Céline Varvenne and Emmanuel Clouet, "Elastic dipoles of point defects from atomistic simulations," Phys. Rev. B **96**, 224103 (2017).

[43] P. J. Brown, A. G. Fox, E. N. Maslen, M. A. O'Keefe, and B. T. M. Willis, "Intensity of diffracted intensities," International Tables for Crystallography **C**, 544 – 595 (2006).